Published in final edited form as:
Phys Rev A. 2014 August 6; 90(2): 023406–.

Characterizing and modeling the efficiency limits in large-scale production of hyperpolarized ^{129}Xe

M.S. Freeman[1,2], **K. Emami**[3], and **B. Driehuys**[1,2]

[1]Center for In Vivo Microscopy, Department of Radiology, Duke University, 311 Research Drive, Durham, NC, 27710, USA

[2]Medical Physics Graduate Program, Duke University, 2424 Erwin Rd, Ste. 101, Durham, NC, 27710, USA

[3]Polarean, Inc., 2500 Meridian Pkwy #175, Durham, NC 27713, USA

Abstract

The ability to produce liter volumes of highly spin-polarized ^{129}Xe enables a wide range of investigations, most notably in the fields of materials science and biomedical MRI. However, for nearly all polarizers built to date, both peak ^{129}Xe polarization and the rate at which it is produced fall far below those predicted by the standard model of Rb metal vapor, spin-exchange optical pumping (SEOP). In this work, we comprehensively characterized a high-volume, flow-through ^{129}Xe polarizer using three different SEOP cells with internal volumes of 100, 200 and 300 cc and two types of optical sources: a broad-spectrum 111-W laser (FWHM = 1.92 nm) and a line-narrowed 71-W laser (FWHM = 0.39 nm). By measuring ^{129}Xe polarization as a function of gas flow rate, we extracted peak polarization and polarization production rate across a wide range of laser absorption levels. Peak polarization for all cells consistently remained a factor of 2-3 times lower than predicted at all absorption levels. Moreover, although production rates increased with laser absorption, they did so much more slowly than predicted by the standard theoretical model and basic spin exchange efficiency arguments. Underperformance was most notable in the smallest optical cells. We propose that all these systematic deviations from theory can be explained by invoking the presence of paramagnetic Rb clusters within the vapor. Cluster formation within saturated alkali vapors is well established and their interaction with resonant laser light was recently shown to create plasma-like conditions. Such cluster systems cause both Rb and ^{129}Xe depolarization, as well as excess photon scattering. These effects were incorporated into the SEOP model by assuming that clusters are activated in proportion to excited-state Rb number density and by further estimating physically reasonable values for the nanocluster-induced, velocity-averaged spin-destruction cross-section for Rb ($\langle\sigma_{\text{cluster-Rb}}v\rangle \approx 4\times10^{-7}$ cm^{3}s^{-1}), ^{129}Xe relaxation cross-section ($\langle\sigma_{\text{cluster-Xe}}v\rangle \approx 4\times10^{-13}$ cm^{3}s^{-1}), and a non-wavelength-specific, photon-scattering cross-section ($\sigma_{\text{cluster}} \approx 1\times10^{-12}$ cm^2). The resulting modified SEOP model now closely matches experimental observations.

I. Introduction

The production of hyperpolarized (HP) ^{129}Xe by spin-exchange optical pumping (SEOP) has led to many applications in scientific and medical research [1]. Polarized ^{129}Xe is used in a variety of studies such as permanent electric dipole moment (EDM) searches [2],

surface characterization [3], protein binding [4], biosensor development [5, 6], cell spectroscopy [7], cross-polarization [8], and, of course, biomedical magnetic resonance imaging (MRI) [9]. Particularly for clinical MRI, where scanner time is limited, HP ^{129}Xe must be generated with both high polarization and high production rate.

The most common approach to ^{129}Xe polarization uses spin-exchange optical pumping, wherein angular momentum is first transferred from laser photons to an alkali metal such as Rb, and subsequent collisions transfer a portion of the absorbed angular momentum to the ^{129}Xe nuclei through a Fermi-contact hyperfine interaction [10]. The primary means to achieve both high polarization and high production rate is to employ a buffer gas mixture lean in ^{129}Xe, flowing continuously through a Rb-filled optical pumping cell illuminated with tens to hundreds of watts of 795-nm laser light, resonant to the D1 absorption of Rb. Hyperpolarized ^{129}Xe is subsequently separated from the other gases by cryogenic extraction [11].

However, since large-scale continuous flow polarizers were first introduced, their performance levels, as measured by both polarization and production rate, have fallen far short of theoretical predictions [11, 12]. The first continuous-flow ^{129}Xe polarizer achieved just 2-5% polarization in volumes of 1 L produced in one hour, while using 140 W of laser light [11]. This stood in stark contrast to predicted polarization levels of 60-80% and production rates of 2.5 L/hr.

Subsequent years saw numerous improvements that should have positively impacted polarizer performance. Initially, laser beam profiles, optics, and optical cell quality were improved so that more power illuminated the optical cell more homogeneously. But little substantial gain was realized. Furthermore, significant improvements in laser performance, such as line narrowing the spectral profile from $\sim$2 nm to $\sim$0.2 nm, did not yield the advantages expected. Even greatly increased laser power [12] led to negligible improvements in both polarization and production rate. Moreover, additional phenomena were reported that could not be readily explained by standard models of SEOP. For example, polarization increased when more N_2 quenching gas was added, or when lasers were detuned from the Rb D1 resonance [13]. Additionally, polarizers operating with richer xenon mixtures and attendant higher spin destruction rates [13], actually exceeded in many cases, the performance of polarizers using lean ^{129}Xe mixtures. Most fundamentally, perhaps the most unrecognized discrepancy has been the inability to increase ^{129}Xe production rate by simply scaling up the laser power.

In principle, ^{129}Xe production rate should increase as more laser light is absorbed by the alkali vapor. As introduced by Bhaskar, et al. [14], the fraction of Rb-^{129}Xe collisions resulting in spin exchange rather than alkali spin destruction, determines the overall efficiency with which circularly polarized photons are converted into nuclear spins. This so-called photon efficiency for ^{129}Xe-Rb spin exchange during binary collisions and short-lived molecular formation [15] was recently re-calculated by Norquay, et al. [16] to be 4.6%. That is, for every Watt of 795 nm light absorbed by the ^{129}Xe-Rb system, it should be feasible to produce 25 mL/hr of polarized ^{129}Xe. Hence, a polarizer absorbing 100 W of laser light

should readily produce 2.5 L/hr, and absorbing 200 W should produce 5 L/hr, and so on. In practice, however, most systems achieve nowhere near their theoretical production rate.

A significant breakthrough came with the work of Ruset et al. [17], who introduced a massively scaled-up polarizer design that also greatly exceeded the performance of all compact designs described previously and since. This work introduced several design changes: 1) a vertical orientation, 2) a large optical cell, ∼1.8 m length, 3) lower pressure operation with line-narrowed lasers, 4) removal of bulk Rb from the cell with pre-saturation of the incoming gas stream with Rb vapor, 5) a cooling region prior to ^{129}Xe exiting the cell, and 6) more gradual cryogenic accumulation. This design also touted a “counter-flow” approach, with ^{129}Xe flowing towards the laser, although this had been a part of every flow-through ^{129}Xe production design ever published [11, 12, 18-22]. However, the improved performance was unassailable—polarizations of 50% and production rates of 1.2 L / hr were achieved.

Although the work of Ruset, et al. represented a clear breakthrough, a fundamental explanation for the improved performance has not yet been provided [23]. Moreover, even this design did not achieve theoretical photon efficiency. A similar system to that of Ruset was thoroughly characterized by Schrank, et al. [21], albeit with more modest 30-W laser power, and this work showed that the alkali polarization was near unity, close to what was predicted by theoretical modeling. Hence, a picture began to emerge that larger polarizer designs employing optical cells with volumes of several liters and operating at relatively cooler temperatures confer a design advantage over the earlier “small and hot” designs that employ optical cells with volumes of a few hundred cc, but operate at higher temperatures and alkali number densities to absorb the available light. Interestingly, the recent work of Nikolaou, et al. represents a second breakthrough [24]. They achieve very high ^{129}Xe polarization, albeit while absorbing very little of the available laser light, and thus limiting production rates. Nonetheless, these demonstrations indicate that regimes exist where ^{129}Xe polarizer performance can approach theory.

This manuscript describes a detailed study of both ^{129}Xe polarization and production rate for a continuous flow polarizer operating with three different cell geometries and two different laser configurations (line-narrowed and free-running). When these results are compared with a standard model of SEOP, it is evident that both polarization and production rate are systematically reduced. We demonstrate that our data can be well explained, if we hypothesize that vapor phase Rb does not consist only of atomic vapor, but also contains nanoscale Rb clusters. Alkali metals are known to form such clusters [25], and their interaction with resonant 795-nm laser light was recently reported to create a plasma-like state [26]. Specifically, we postulate that activated clusters cause both Rb spin destruction and ^{129}Xe spin relaxation, as well as a small degree of unproductive scattering of incident laser photons. When the effects of these clusters are incorporated into the standard model, the observed polarizer performance agrees with the new model to a remarkable degree.

II. Theoretical Model

A. Standard model of optical pumping

A means to model the SEOP process was introduced by Wagshul and Chupp [27] in 1989, and was recently updated by Norquay, et al. to include the latest measured spin exchange and spin destruction cross-sections for ^{129}Xe [16]. We use this as the "standard model" with two minor changes (see Appendix). Because it was recently described in detail, we reiterate only the key elements here. Briefly, the alkali metal polarization is calculated as a function of position *z* in the optical cell along the laser propagation direction according to

$$P_{Rb}(z)=\frac{\gamma_{OP}(z)}{\gamma_{OP}(z)+\Gamma_{SD}}, \quad (1)$$

where Γ_{SD} is the alkali spin destruction rate, caused by collisions of Rb with other gas species within the cell, which for binary collisions is defined by

$$\Gamma_{SD}^{binary}=\sum_i [G_i]\kappa_{SD}^{Rb-i}, \quad (2)$$

with spin-destruction coefficients κ_{SD}^{Rb-Rb}, κ_{SD}^{Rb-He}, $\kappa_{SD}^{Rb-N_2}$ and κ_{SD}^{Rb-Xe} [15]. The optical pumping rate γ_{OP}(z) is, determined by the overlap of the frequency- and position-dependent laser intensity profile $\Phi(\nu,z)$ and the alkali D1 absorption cross-section $\sigma_s(\nu)$ according to

$$\gamma_{opt}(z)=\int_0^\infty \Phi(\nu,z)\sigma_s(\nu)d\nu. \quad (3)$$

In this one-dimensional model, photons are removed from the propagating light at each step, Δ*z*, through the optical cell, according to

$$\frac{d\Phi(\nu,z)}{dz}=-[Rb]\cdot\Phi(\nu,z)\cdot\sigma_s(\nu)\cdot(1-P_{Rb}(z)) \quad (4)$$

Where [Rb] is the alkali number density. The alkali absorption cross-section $\sigma_s(\nu)$ is taken as a Lorentzian

$$\sigma_s(\nu)=\frac{2cr_e f_{osc}}{\Gamma_{fwhm}}\frac{(\Gamma_{fwhm}/2)^2}{(\nu-\nu_0)^2+(\Gamma_{fwhm}/2)^2} \quad (5)$$

where *c* is the speed of light, r_e is the electron classical radius, f_{osc} is the oscillator strength, which we take as 0.322 for the D1 transition of Rb [28]. The cross-section is maximum at its resonant frequency ν_0, while Γ_{fwhm} is the full width at half max of the distribution. Γ_{fwhm} is calculated using known pressure-broadening coefficients for Rb with the buffer gases He, Xe, and N_2 [29], which are all on the order of ~18 GHz/amg.

The photon flux is modeled as a roughly Gaussian function of frequency according to

$$\Phi(\nu)=\frac{P_{lsr}}{h\nu_0 A_{lsr}\delta\nu_{fwhm}}\sqrt{\frac{4\ln 2}{\pi}}e^{-4\ln 2\left(\frac{\nu-\nu_0}{\delta\nu_{FWHM}}\right)^2} \quad (6)$$

where P_{lsr} is the laser power, distributed over an area A_{lsr}, $h\nu_0$ is the photon energy, and $\delta\nu_{FWHM}$ is the full width half maximum of the laser distribution.

^{129}Xe becomes polarized by spin-exchange collisions with the polarized Rb atoms at a rate $\gamma_{SE} = \kappa_{SE}[Rb]$, where κ_{SE} is a rate constant that includes contributions from both binary collisions and pressure-dependent short-lived molecular formation [16]. We assume ^{129}Xe interacts with a volume-averaged polarization $\langle P_{Rb}\rangle$, which is appropriate for the cell volumes and geometries considered in this paper, in which the flowing gas mixture should be highly turbulent [30]. Hence, ^{129}Xe polarization as a function of time is

$$P_{Xe}(t_{res})=\gamma_{SE}\tau_{SU}\langle P_{Rb}\rangle\left(1-e^{-t_{res}/\tau_{SU}}\right) \quad (7)$$

where t_{res} is the mean ^{129}Xe residence time in the optical cell, and τ_{SU} is defined as

$$\frac{1}{\tau_{SU}}=\gamma_{SE}+\Gamma_1 \quad (8)$$

where Γ_1 is the ^{129}Xe relaxation rate. For the purposes of practically characterizing the output of a flow-through polarizer, it is convenient to cast this expression in terms of the mass flow rate, F, through the optical cell, which is related to Xe residence time therein according to $t_{res} = V_{cell}[G]/F$, where V_{cell} is the cell volume and [G] is the total gas density in the cell, in amagats. This allows us to write Equation 7 as

$$P_{Xe}(F)=P_0(1-e^{-F_{crit}/F}) \quad (9)$$

where F_{crit} is the critical flow rate at which Xe atoms spend, on average, one spin-up time constant, τ_{SU}, in the optical cell before exiting, and P_0 describes the peak ^{129}Xe polarization at zero flow. This then permits us to simply define the ^{129}Xe production rate as the $F_{Xe} = f \times F_{crit}$ where f is the fraction of xenon in the gas mixture.

III. Experiment

A. Quantifying performance

All experiments were performed on a commercially available polarizer (Model 9800, Polarean, Inc., Durham, NC), fitted either with the standard 300-cc SEOP cell, or retrofitted with custom-designed alternative cells with internal volumes of 100 or 200 cc. To measure the effects of laser narrowing, two different fiber-coupled diode laser arrays were used: a broad-band, 111 W, 1.92 nm FWHM laser (Dual FAP, Coherent, Inc., Santa Clara, CA), and the second, a line-narrowed, 71-W, 0.39-nm FWHM laser (QPC Lasers, Laser Operations

LLC, Sylmar, CA). Light from these systems was coupled via a 200-cm fiber optic to an optics box that collimated the beam, split it into horizontally and linearly polarized components, and circularly polarized each. The two beams were adjusted to maximize light transfer to the cells such that the beam that did not pass straight through the polarizing beam splitter entered the cell at a 7° angle and intersected the straight beam at the cell mid-point. We estimate that for the broad laser, 94 W of light was coupled into the cell, and for the narrowed laser, 60 W were coupled in. This 15% reduction in incident photon intensity results from reflective losses at the glass interfaces on the oven window and cell face. The measured cold cell wall relaxation times for each cell are listed in Table I.

For each combination of laser and optical cell, ^{129}Xe polarizations vs. gas-flow curves were acquired with increasing degrees of laser absorption. A gas mixture, consisting of 1% Xe (natural abundance), 10% N_2, and 89% ^{4}He flowed through the optical cell at 6 atm pressure. Upon exiting the cell, the gas mixture was directed via a 150-cm length of 6.4-mm O.D. polyurethane tubing to a ∼50-cc test bulb housed in a volume NMR coil in the center of a polarization measurement station (Polarean, Inc., Model 2881). This system acquires ^{129}Xe NMR at 25 kHz and has sufficient sensitivity to detect ^{129}Xe polarized to 25%, within the dilute 1% mixture, with a single shot SNR of ∼20. A diagram of the experimental configuration is shown in Figure 1.

To measure polarization as a function of flow, the system was first allowed to equilibrate to the desired laser absorption level, while gas flowed slowly at 0.20 SLM (2.0 sccm Xe). Once absorption was stable, flow was continued for a time $1.5\times t_{res}$ before being stopped, and acquiring four ^{129}Xe NMR signals from the test bulb using a series of four 22° pulses. The 4×-averaged free-induction decays (FIDs) were line-broadened by 0.10 Hz, Fourier transformed, and quantified by their peak height. The flow was then restarted, and ^{129}Xe NMR measurements were made at successively higher flow rates in increments of 1.0 sccm up to 10 sccm, and then 2.0 sccm up to 20 sccm, and increments of 4.0 sccm up to 36 sccm. At each flow rate, polarization was permitted to equilibrate for $1.5\times t_{res}$ prior to taking ^{129}Xe polarization measurements.

1. Converting NMR signal to absolute polarization—To convert the signal attained within the test bulb to a quantifiable polarization, a calibration was done by simultaneously dispensing pure xenon polarized to ∼10% into the bulb and a 300-cc Tedlar bag at atmospheric pressure. The bag was then placed on a second, calibrated measurement station to determine its absolute polarization. This station was originally calibrated against thermally polarized ^1H_2O, and is recalibrated annually using a calibration transfer standard [31]. Combined with measured signal from ^{129}Xe in the flow test station, this provided a calibration constant that required only scaling for ^{129}Xe density during polarization vs. flow tests.

IV. Data and Analysis

A. Flow curves and the standard model

Figure 2 depicts a series of representative polarization vs. flow curves acquired using the line-narrowed laser illuminating a standard 300-cc optical cell, at 50-100% absorption. A

few trends are evident from these curves. When operating at 50% laser absorption, we observe a peak polarization of 23 ± 2%, and a xenon production rate of 12 ± 3 sccm. As absorption increases to 80%, the peak polarization reaches a maximum of 29%, before beginning to drop modestly as xenon production rate begins to increase. For the highest 100% absorption, the peak polarization decreases to 20 ± 6%, while production rate increases to 34 ± 9 sccm. The general trend of increasing production rate with increasing light absorption is qualitatively consistent with expectations from photon efficiency arguments, although the relatively low polarization and its limited variation with absorption are not consistent.

B. Comparison to the standard model

Figures 3 and 4 show plots of peak ^{129}Xe polarization and xenon production rate ($f \times F_{crit}$) as a function of laser absorption for all combinations of cell geometry and laser configuration. These plots have superimposed on them the theoretically predicted polarization levels and production rates determined using the standard SEOP model. These comparisons across a range of laser absorptions illustrate a clear and systematic discrepancy between observed data and model predictions. Beginning with the 300-cc cell pumped with the line-narrowed laser, we note at low absorption, ^{129}Xe polarization is nearly 3-fold lower than predicted. This polarization gap narrows to roughly 2-fold at the highest absorptions. However, xenon production rate appears to agree very well with prediction and increases with absorption as expected.

When the same 300-cc cell is pumped with the broad-spectrum laser, peak ^{129}Xe polarization is nearly 2-fold lower than predicted at low absorption, but approaches the model at higher absorptions. The production rate for this laser/cell combination matches model predictions at low absorption, but deviates significantly below predictions at the higher absorption levels. For the broad laser, the standard model predicts high xenon production rates as absorption increases because it requires absorbing the most off-resonant photons, which can only happen at very high [Rb], given the small off-resonance cross-section. High [Rb], in turn, would yield high spin exchange rates and hence high production rates. However, such high production rates are not seen for the broad laser, suggesting other photon-scattering mechanisms may be coming into play.

Inspection of ^{129}Xe polarization for the smaller 200- and 100-cc cells show similar discrepancies with the model predictions for both laser configurations. When pumping with the broad laser, ^{129}Xe polarization again starts roughly 2× below predictions at low absorption, with slight convergence towards model predictions at higher absorptions, although less so than seen with the 300-cc cell. For the narrowed laser, the ^{129}Xe polarization discrepancy with the model is greater and remains consistently so across the range of absorption values. Observing such low ^{129}Xe polarization, even as the available laser light is being concentrated over progressively smaller areas, is suggestive of a mechanism whereby increasing laser intensity is not productively deployed to produce polarized ^{129}Xe.

An additional discrepancy between model and measured data lies in the reduced ^{129}Xe production rates obtained with the smaller 200-cc and 100-cc cells. When pumping with the

broad laser, xenon production rate is close to expectations for both cells at low absorption. However, as absorption increases, the observed production is significantly lower than model predictions. When pumping with the narrowed laser, the production rate for these smaller cells remains consistently a factor of two below model predictions. For example, when absorbing 50% of narrowed light, the 200-cc cell produces just 12 ± 2 sccm of HP xenon, whereas roughly twice that value is predicted. This underproduction remains roughly 2-fold below predicted values across the entire range of absorption for the narrowed laser. These findings suggest that despite concentrating the available light into smaller volume cells, the resulting absorption and/or scattering of higher intensity laser light is not being fully converted into production of polarized ^{129}Xe nuclei.

The diminished ^{129}Xe production achieved using smaller cells relative to larger ones is perhaps best illustrated in Figure 5, which compares polarization vs. flow curves acquired at 50% absorption of narrowed light in the 300-cc cell and the 100-cc cell. Note the peak polarization in the smaller cell is 52 ± 4%, vs. 23 ± 2% in the larger cell. This result is somewhat consistent with the expectation that concentrating the available light on the 2× smaller cell area results in 2× greater optical pumping rate, and thus higher alkali polarization. However, at such relatively low absorption, pumping rate is not expected to limit alkali polarization; the predicted volume averaged alkali polarizations in these cells are 91% (100-cc cell) and 85% (300-cc cell) at 50% absorption. The more striking finding is that while these cells absorb essentially the same amount of laser power (∼30 W), the production rate is decreased by 4-fold in the small cell (3 ± 1 sccm) relative to the 300-cc cell (12 ± 3 sccm). Thus, a simple geometric change that concentrates more laser light in a smaller volume, and requires operating at higher alkali vapor pressures to absorb that light appears to grossly reduce the photon efficiency of the system.

C. Possible extensions to the standard model of SEOP

The extensive characterization of 6 different cell geometry and laser combinations across a wide range of absorption conditions provides a means to evaluate and extend the “standard model” of ^{129}Xe SEOP to better account for underperformance. Thus, we seek to postulate an effect or series of effects that could augment the standard model such that predicted performance is brought in line with our findings across all combinations of cell and laser. Such an exercise has value because it may provide the insights into the mechanisms that have lead to chronic underperformance of this and other polarizer designs. Once a model has been proposed, it is subject to testing and developing a robust means to suppress such mechanisms to regain the efficiency predicted by the standard theory. This would permit the rational design of polarizers based on fundamental insights rather than serendipitous design modifications.

To date, a large number of mechanisms have been proposed that in some way impede the efficiency of SEOP. The bulk of these mechanisms have been introduced in the context of ^{3}He-Rb SEOP. These include a) $P_{3/2}$ mixing and D2 pumping [32], b) hypothesizing a less than unity alkali polarization limit [33], c) long-range dipolar spin-exchange interactions, d) radiation trapping [34, 35], e) energy pooling collisions [36], f) temperature-dependent spin destruction [16], g) imperfect circular polarization [37], or h) skew light

optical pumping [38]. Each of these effects may be playing a role, but fail to explain our range of results. Specifically, none explain the poor ^{129}Xe polarization at low absorption levels, and its relatively unchanged nature as absorption increases. Moreover, none fully explain the utter lack of benefit resulting from spectrally narrowed laser light, and very poor production rates obtained when concentrating light into smaller optical cells.

Our results are also not readily explained by more pedestrian mechanisms. For example, one might consider whether poor quality optical interfaces simply lead to far less laser power entering the cell than expected. While this could again explain poor performance at high absorption, even small amounts of laser power should still generate high ^{129}Xe polarization at low absorption, given the very dilute xenon mixture we employ. But, this is not observed. Particularly the narrowed laser, even at very low power, should generate exceedingly high alkali polarization, and by extension very high ^{129}Xe polarization. In fact, such high alkali polarization was confirmed by Schrank, et al. [21] in characterizing a variant of the Ruset polarizer using only 30 W. Thus, it might become tempting to explain the ^{129}Xe polarization at low absorption (low temperature), by invoking an exceedingly short ^{129}Xe wall relaxation time. However, this would require cold wall relaxation times on the order of 2 min, whereas we measured T1s ranging from 8-56 min for the cells used in this study (see Table I). Moreover, even if such a short wall relaxation time were present, then ^{129}Xe polarization should increase dramatically at higher light absorption, where [Rb] increases and spin exchange rates begin to exceed wall relaxation rates. But in fact, particularly for the narrowed laser case, ^{129}Xe polarization is almost flat across all absorptions. Thus, the mechanism responsible for suppressing ^{129}Xe polarization at low absorption appears to become steadily stronger at higher absorption, such that it cannot be overcome by faster spin exchange rates.

D. Hypothesizing laser induced generation and activation of Rb clusters

The observations and analysis presented thus far point to the need to extend the standard SEOP model in two ways. First, we require a mechanism that dramatically suppresses the ^{129}Xe polarization at low absorption. It must do so, while still permitting high alkali polarization at low absorption, as measured by Schrank and co-workers [21]. Thus, we suggest the presence of a highly paramagnetic, unpolarized species that rapidly relaxes ^{129}Xe. Moreover, to explain the lack of improvement in polarization at higher laser absorption, this mechanism must intensify with absorption. A second requirement is that it must somehow disproportionately punish the higher optical pumping efficiency of the narrowed laser relative to the broad one. But given literature reports of exceedingly high ^{129}Xe polarization achieved in polarizers running in different regimes than we describe here, it must also be possible to remove or suppress these mechanisms through design changes. And finally, we require a mechanism that scatters off-resonant laser photons much more potently than atomic Rb. This is required to account for the remarkably efficient loss of light from the wings of the broad laser, which are depleted at far lower temperature, and thus lower [Rb] than predicted.

Based on these requirements, we hypothesize that the deleterious effects we observe are caused by the formation of many-atom Rb clusters. Although, rarely discussed in the optical

pumping literature, clusters have long been known to form in dense, supersaturated alkali metal vapors [21]. Moreover, alkali clusters have been shown to be paramagnetic, with an overall magnetic moment that increases with cluster size [39]. Of particular relevance for flow-through SEOP systems where some impurities are unavoidably introduced over time, incorporation of other atoms can enhance cluster magnetic moments [40]. Particularly, incorporation of oxygen atoms into Rb clusters produces a large magnetic moment [41]. Furthermore, given their high free-electron densities, alkali clusters exhibit broad (>50 nm FWHM) light scattering. Such scattering has been studied in sodium clusters and has shown to be driven by the collective resonances of the valence electrons, which exhibit a photon-absorption cross-section that depends on cluster size [42].

The study of alkali clusters has exploited numerous methods to deliberately promote their formation. Commonly, Rb clusters are formed by heating a Rb pool to ∼600 K to create a high vapor pressure and then flowing a cool noble gas over it to create a supersaturated condition that causes the alkali atoms to aggregate into clusters. Interestingly Rb cluster sizes favor a distribution derived from a shell structure, which for Rb results in favored sizes with n = 3, 9, 19, 21, 35, 41, etc. atoms [43]. Again, the likely introduction of O_2 impurities and reaction with atomic Rb vapor would both diminish the energy requirements for and promote formation of larger clusters at more modest temperatures [44].

Given an abundance of approaches for deliberate creation of alkali clusters, it is not difficult to imagine their unintended presence in SEOP cells. However, it is somewhat more challenging to delineate an exact mechanism by which they arise and how laser light may aid their formation or activation. One possible effect of the laser is to promote light induced atomic desorption (LIAD), wherein atomic Rb is desorbed from a surface by non-wavelength specific light [45]. In fact, in our SEOP cells we notice that within seconds of turning on the laser, 5-10% of the incident light is already absorbed. Although LIAD typically involves desorbing alkalis from polymer coated cells [46] or those containing porous silica [47], it may also occur to a modest extent in uncoated cells, especially in the presence of 10's to 100's of watts of light and macroscopic pools of Rb. Such localized increases in vapor pressure would be met in a flow-through SEOP cell, by cool gas mixture entering the cell and create localized supersaturation that begins the aggregation process.

The role of the laser continues once clusters have been formed. As recently shown by Atutov, et al. [26], the incidence of 1 $W \cdot cm^{-2}$ of D1 resonant light causes clusters to become unstable and to explode. Atutov, et al. observed Rb clusters exploding, fluorescing, and propagating in a soliton-like fashion through a hot, buffer-gas filled heat-pipe optical cell. Atutov describes these exploded clusters as exhibiting a very hot plasma-like state involving significant numbers of free electrons, which would be highly depolarizing. Multiply ionized clusters have temperatures approaching their boiling point, and atoms within the cluster behave like a liquid [48]. Beyond this point, as clusters ionize further, their internal energy causes them to explode. It is particularly noteworthy that Atutov noticed that incident light had to be to be within 5 GHz of the D1 resonance to cause clusters to fragment.

The emerging picture of cluster formation and destruction by laser light may also play a role in the commonly observed phenomena of “rubidium runaway” in ^{129}Xe SEOP systems [49,

50]. The formation of Rb clusters would likely be concentrated near high-intensity laser irradiation of alkali metal atoms near bulk alkali pools on the optical cell surface. The LIAD effect creates localized high vapor pressure, which when combined with the flow of cool gas or convection creates a supersaturated vapor that promotes particle agglomeration. Subsequent irradiation of clusters by resonant D1 light causes cluster explosion into vapor, with increased heating, and further supersaturation. Thus, one can conceive of a rapid and dynamic cycle, wherein clusters are formed, absorb energy, release electrons into a plasma-like state, and energetically explode. Alkali vapor and fragments are eventually incorporated into new clusters and are convectively dispersed throughout the vapor in the SEOP cell.

1. Modeling Rb clusters—With this background in mind, we seek to model the clusters in the simplest possible way until such time that they may be better characterized. To simplify the complex dynamic state of clusters and calculate their effects on polarization, we refer to them at any point within their formation and destruction cycle as “activated” clusters. Such clusters would have several effects. First, the presence of these large, paramagnetic clusters and related plasmas must relax ^{129}Xe nuclei. We model this process simply as collisional relaxation between ^{129}Xe and the cluster according to

$$\frac{1}{T_{1Xe}} = [Rb_n^{z+}]\langle \sigma_{cluster-Xe} v \rangle \quad (10)$$

where $[Rb_n^{z+}]$ is the activated cluster number density, in which n signifies the unknown, but non-negligible, number of atoms in the cluster, and z+ signifies its unknown, but non-negligible, ionization state. And, akin to spin exchange formalism, $\langle \sigma_{cluster-Xe}\ v \rangle$ is the velocity-averaged relaxation cross-section for ^{129}Xe-cluster collisions. Given their large size, Rb_n^{z+} clusters should exhibit a much larger collisional cross-section with ^{129}Xe than would their atomic Rb counterparts. Estimates of Rb cluster size from the literature, range from ∼40 nm when formed at very low buffer gas pressure [51], to ∼600 nm when formed at higher pressure and irradiated with ∼ 1 W·cm^{-2} of D1 resonant light [26]. With these geometrical considerations in mind, we estimate the cross-section for ^{129}Xe atoms colliding with Rb clusters to be 4-6 orders of magnitude larger than for atomic Rb. Assuming a less efficient spin interaction than for atomic Rb-^{129}Xe, and through further steepest descent tuning detailed below, we arrive at an estimated velocity-averaged cross-section of $\langle \sigma_{cluster-Xe}\ v \rangle \approx 4\times10^{-13}\ cm^3 s^{-1}$. This is roughly 3 orders of magnitude larger than the measured Rb-^{129}Xe velocity-averaged spin-exchange cross-section. Thus, even a small number density of clusters could begin to compete with spin exchange to suppress ^{129}Xe polarization.

If activated Rb clusters have a relaxing effect on ^{129}Xe, they must also cause Rb spin destruction. We characterize this spin destruction using the same standard collisional formalism

$$\Gamma_{SD_{clusters}} = [Rb_n^{z+}]\langle \sigma_{cluster-Rb} v \rangle \quad (11)$$

where $\langle \sigma_{cluster-Rb}\, v \rangle$ is the velocity-averaged Rb relaxation cross-section induced by cluster collisions. Through similar estimates as outlined above we estimate this cross-section to be $\langle \sigma_{cluster-Rb}\, v \rangle \approx 4\times10^{-7}\, cm^3 s^{-1}$. By comparison, the atomic Rb-Rb spin destruction cross-section is $\langle \sigma_{Rb-Rb} \rangle = 4.2\times10^{-13}\, cm^3 s^{-1}$ [52]. Again, the relatively larger size of clusters would endow them with comparatively enormous collisional cross-sections relative to pure atom-atom interactions.

And finally, we model the broadband scattering of laser photons by clusters by endowing them with a wavelength-independent scattering cross-section that wastes photons in proportion to their density, $[Rb_n^{z+}]$. Again using the steepest-descent optimization described below, we estimate this scattering cross-section to be

$$\sigma_{cluster} \approx 1 \times 10^{-12} cm^2, \quad (12)$$

which is roughly an order of magnitude larger than the peak scattering cross-section for the atomic Rb D1 resonance under the conditions in our cell. This estimate substitutes for what is likely to be an overlap of many Mie-scattering profiles arising from a broad distribution of cluster sizes.

With the physical effects of activated clusters included in the model, the remaining task is to postulate a means of scaling their number density. We seek to account for two factors that we have empirically observed to diminish polarizer performance. The first, is that neither polarization nor production rate improve when laser intensity increases or spectral width is narrowed. Second, higher alkali vapor pressure in smaller cells appears to negatively impact performance. For these reasons, we model cluster density as being proportional to excited state Rb population. This incorporates increased optical pumping rate (through either narrowing or concentrating laser light), increased spin destruction rates, and higher alkali vapor pressure into the cluster generation mechanism. Note, that this approach has been empirically found to best explain our measurements. We also attempted to scale cluster number density according to Rb number density alone, optical pumping rate alone, gas temperature, and photon intensity. None of these approaches agreed with observation to the same extent. The excited state Rb density is given by

$$[Rb_{5p+^1/_2}] = \tau \cdot \gamma_{OP} \cdot [Rb] \cdot (1 - P_{Rb}) \quad (13)$$

where τ is the excited state lifetime. Substituting for P_{Rb} as defined in Equation 1 into Equation 13, and subsuming the lifetime into the overall scaling constant $\Theta_{cluster}$ we obtain an expression for cluster density as a function of alkali density of

$$[Rb_n^{z+}] = \Theta_{cluster} \cdot \left(\frac{\gamma_{OP}\Gamma_{SD}}{\gamma_{OP}+\Gamma_{SD}} \right) \cdot [Rb]. \quad (14)$$

This way of modeling cluster number density $[Rb_n^{z+}]$ thus increases as a function of [Rb], as well as γ_{OP} and Γ_{SD}. This approach appears to appropriately punish operating at higher

alkali number density, as well as penalizing high optical pumping rates achieved by laser narrowing or concentrating power in a smaller volume. We should note, however, that the overall scaling of activated cluster number density and the postulated cross-sections are not fully independent. Thus, the same modeling effect can be achieved by increasing cluster density and decreasing the associated cross-sections, or vice versa. Thus, as a starting point for the model we have set the overall scale such that $[Rb_n^{z+}]$, is roughly $^1/_{1000}$ the number density of atomic Rb at 100°C. This gives us a starting constant $\Theta_{cluster} = 6.5\times10^{-8}s$.

E. Steepest descent tuning of cluster parameters

To arrive at the best possible estimates of the associated cross-sections and number density scaling, we wish to "fit" the entirety of our collected dataset. However, since this data does not have a simple analytical function, an alternative approach is to use a steepest descent gradient fitting routine to minimize least squares differences with the model results. We allowed only three model parameters to be adjusted: $\langle\sigma_{cluster-Rb}\ v\rangle$, $\langle\sigma_{cluster-Xe}\ v\rangle$ and $\sigma_{cluster}$. These same parameters were used to collectively fit the entire data set, including polarization and production rate at all absorption levels, for all six combinations of cell geometry and laser configuration. Prior to running the steepest descent gradient algorithm, a baseline starting-guess for all the parameters was adjusted until the predictions of the model came into good visual agreement with the data. Then, a random number generator varied all six values between 0× and 2× the values found in the qualitative fit, 51,751 times. The best fit from that sequence was then run through a steepest descent gradient fitting routine to further optimize the parameters toward a global minimum. The technique used a cost function consisting of a least squares difference between the 24 polarization data points and numerical model, as well as the differences for the 24 production rate data points and the model.

F. Results of steepest descent modeling

The results of the steepest descent fits appear in Fig. 6 showing peak polarization data compared to the optimized model, and Fig. 7 showing production rate compared to the optimized model. Note that peak polarization now agrees well across the entire range of absorptions for all six combinations of laser and optical cell geometry. Particularly, the low-absorption polarization, which so greatly underperforms the standard model, is now pulled into line by cluster-induced relaxation of the ^{129}Xe. This mechanism of polarization suppression continues to grow towards higher absorption levels. The model also appears to better predict the observed production rates (Fig. 7). For the narrowed laser, the model correctly predicts the poorer photon efficiency for the smaller optical cells. For the broad laser, the model now does a good job of slowing the predicted production rates at higher absorption levels. The hypothetical cluster cross-sections used to generate these curves are listed in Table II.

G. Comparison of individual cluster effects

The new activated cluster model comes to agreement with data through the addition of three cluster-initiated effects, a velocity-averaged spin destruction cross-section, $\langle\sigma_{cluster-Rb}\ v\rangle$, a velocity-averaged ^{129}Xe relaxation cross-section $\langle\sigma_{cluster-Xe}\ v\rangle$ and a broad photon-

absorption cross-section $\sigma_{cluster}$. To appreciate the individual influence of each of these mechanisms, their effect on predicted polarization and production rate are shown in Figs. 8 and 9. For these figures the standard model was run, while adding in only one additional effect at a time (red for spin destruction, green for light scattering and blue for ^{129}Xe relaxation), and compared against the full cluster model (black).

1. Spin destruction—When only the effect of cluster-induced spin destruction on the atomic Rb is added to the standard model (shown in red in Figs. 8 and 9), it effectively reduces ^{129}Xe polarization at higher laser absorptions levels, but has relatively little effect at the lower absorption levels. Hence, alkali polarization can remain high at low absorption levels, consistent with the findings of Schrank, et al [21]. Cluster-induced alkali spin destruction at high absorption has a more deleterious effect on ^{129}Xe polarization for the broad laser than the narrowed laser. That is because high absorption occurs at higher [Rb] for the broad laser, and clusters grow in proportion to [Rb].

Regarding production rate, the cluster-induced spin destruction, again has little impact at low absorption on any cell configuration. However, as absorption increases, increased alkali spin destruction suppresses production rate more significantly for the narrowed laser than for the broad laser. The narrowed laser, with its higher optical pumping rate, creates a higher cluster number density. This in turn results in a larger fraction of atomic Rb relaxation coming from collisions other than ^{129}Xe-Rb spin exchange collisions. Thus, cluster-induced spin Rb destruction undermines photon efficiency.

2. Broad photon scattering—The effect of cluster-related photon scattering (green line) on ^{129}Xe polarization is somewhat similar to that of Rb spin destruction. It again does not significantly suppress ^{129}Xe polarization at low absorption, but has its most substantial impact at the higher absorption levels. It has a primary effect of decreasing production rates across the board, as laser photons are being unproductively scattered rather than pumping atomic Rb. In fact, for all cell and laser combinations, this effect actually suppresses production rate *below* the rate seen in the final model. That is because in the final model the production rate is actually artificially enhanced partially by exceedingly short ^{129}Xe T1, discussed in the next section. The photon-scattering term was necessary to enable predicting *both* ^{129}Xe polarization and production rate for all combinations of cell and laser.

3. ^{129}Xe relaxation—Cluster-induced ^{129}Xe spin relaxation (blue line) actually appears to provide the bulk of the polarization-limiting effects. For the example of the 100-cc SEOP cell pumped by the broad laser, the ^{129}Xe relaxation time T1 caused by clusters at only 10% absorption is 2 minutes. By the time 90% absorption is reached the ^{129}Xe T1 has been reduced to only 8 seconds. As mentioned, this short ^{129}Xe T1 actually artificially increases apparent production rates, much like the way in which ^{3}He cells with very poor wall relaxation times actually exhibit accelerated spin-up times. In this case, the artificially accelerated production rates are somewhat counterbalanced by the even slower than predicted production rates from true atomic Rb-^{129}Xe spin exchange.

H. Possible presence of activated clusters in ^{3}He cells

Although the work presented here is focused entirely on ^{129}Xe polarization, it is tempting to consider the possibility that clusters may also play a role in ^{3}He SEOP. ^{3}He polarization, although typically quite high, remains plagued by an "X-factor" [53, 54], which behaves somewhat like a temperature-dependent wall relaxation rate that causes cell-to-cell performance variations and scales loosely with their surface-to-volume ratio. Moreover, although impressive ^{3}He polarization levels exceeding 80% are now routinely attained [55], these systems still consume considerably more laser light than should be necessary. Such observations could potentially also be attributable to cluster formation. For example, cluster-induced relaxation of ^{3}He could be difficult to distinguish from enhanced wall relaxation, and clusters could also be responsible for excessive scattering of laser light. However, as we have modeled their formation, cluster generation should be considerably weaker in ^{3}He cells than ^{129}Xe cells. That is because alkali spin destruction in ^{3}He cells is orders of magnitude lower than in ^{129}Xe cells. Thus, excited state Rb density should be considerably lower in ^{3}He cells and cluster number density, as estimated by Equation 14, would be reduced. Moreover, ^{3}He SEOP does not involve flow. It takes place in an ultra-pure environment with uniform temperature, which reduces the conditions of alkali supersaturation that are promoted by cool gas flowing into a hot cell. Absence of flow also diminishes the introduction of contaminants like O_2 and H_2O. Without such contaminants, cluster formation is likely inhibited and cluster size is likely reduced [44]. Nonetheless, the arguments presented here certainly suggest that the Rb cluster formation could be occurring in ^{3}He SEOP, as well.

V. Discussion and Conclusions

A large body of literature describing high-volume production of hyperpolarized ^{129}Xe and ^{3}He is pointing towards a picture that the standard model of SEOP is missing a key component needed to explain observed performance. By postulating the generation of spin destroying, ^{129}Xe relaxing, broadly absorbing Rb clusters and including their effects in the model, we are now able to retroactively predict the performance of our existing polarizers under a large variety of conditions. Although the possibility of generating such clusters is bolstered by the observations of Atutov [26], and several decades of alkali cluster literature, it is important to note that we have not yet taken steps to confirm their presence in our SEOP system or any other. However, this relatively simple, and physically plausible mechanism does a remarkably good job of explaining observed performance, not just at a single operating point, but across a wide range of laser absorption, and a wide range of cell and laser combinations.

Of course, we should note that even if Rb cluster formation is confirmed, the proposed model of their formation and effects on ^{129}Xe relaxation, Rb spin destruction, and optical scattering will undoubtedly be found to be overly simplistic, and the resulting cross-sections only crude approximations. In fact, it is unlikely that such clusters would even form with a uniform size, but instead would likely exhibit a distribution of sizes. However, it stands to reason that some aspects of these three behaviors will be found to persist and their effects to manifest themselves at least qualitatively as postulated here.

One approach to aid in the search for clusters would be to exploit their non-resonant scattering properties. For example, a cell during optical pumping could be interrogated with a broad-spectrum white-light source delivered transverse to the optical pumping direction. The resulting extinction spectra may show characteristic Mie scattering from clusters, and perhaps enable reporting on approximate cluster size [51]. Alternatively, fluorescence spectra reflecting emission of photons from de-excitation of clusters or fragments could represent a second approach to their detection [36].

It is clear that if methods can be developed to directly detect the presence of Rb clusters, the door should be opened to their systematic elimination from SEOP systems. In fact, the recently published results of Nikolaou, et al. [24] already provide encouragement that this can be achieved. This polarizer, operating at very low temperatures and number densities compared to continuous flow polarizers appears to be one of the few with ^{129}Xe polarization that is entirely in line with the predictions of the standard model. This provides encouragement that elimination of clusters from large-scale polarized ^{129}Xe production will result in the ability to routinely and cost-effectively build ^{129}Xe polarization systems that produce liters of polarized ^{129}Xe on-demand at polarizations exceeding 50%.

Acknowledgments

This study was funded by NIH/NHLBI (R01 HL105643) and NCI R01 CA142842. The work was performed at the Duke Center for In Vivo Microscopy, an (NIH/NIBIB) National Biomedical Technology Resource Center (P41 EB015897). The authors thank Zackary Cleveland for helpful discussions and Sally Zimney for carefully reading the manuscript.

Appendix: Modifications to The Standard Model as Reported by Norquay, et al.

The basic premise of the standard model used in this work is identical to that outlined by Norquay, et al. [16]. However, we have made two modifications with regard to calculating Rb spin destruction and the effects of van der Waals molecules. First, we found it necessary to change the way in which temperature dependence of three of the binary spin-destruction coefficients (κ_{SD}^{Rb-He}, $\kappa_{SD}^{Rb-N_2}$ and κ_{SD}^{Rb-Xe}) is used to calculate the binary spin-destruction rate as defined by Eq. 2. While their spin destruction coefficients for He and N_2 scale with absolute temperature (K), as is customary, they scale Xe-Rb spin destruction in Celsius. This may have been an error, because it would imply zero spin destruction at 0° C and negative spin destruction below that temperature.

Thus, we adopt the commonly used method of scaling with $\left({}^{T}/_{298K}\right)^{X}$. Using the most recent literature values we use the temperature-dependent spin destruction coefficients of $\kappa_{SD}^{Rb-He}=3.45\times10^{-19}\cdot\left({}^{T}/_{298K}\right)^{4.26}cm^3s^{-1}$ [52], $\kappa_{SD}^{Rb-N_2}=3.44\times10^{-18}\cdot\left({}^{T}/_{298K}\right)^{3}cm^3s^{-1}$ [56] and $\kappa_{SD}^{Rb-Xe}=6.02\times10^{-15}\cdot\left({}^{T}/_{298K}\right)^{1.17}cm^3s^{-1}$ [15]. Note that this form has the added benefit that the coefficients preceding the temperature term represent the room-temperature value of the parameter of interest, and thus provides some intuitive value.

Moreover, for an abundance of clarity, we express the equation for spin exchange induced by van der Waals molecules introduced by Norquay [57] in the following format:

$$\gamma_{SE}^{\nu dW} \frac{[Rb]}{\sum_i \left(\frac{[G_i]}{\xi_i}\right)}, \quad (15)$$

and use the values for ξ, the van der Waals-specific rates, for He, N_2, and Xe as reported by Norquay.

References

1. Goodson BM. J Magn Reson. 2002; 155:157. [PubMed: 12036331]
2. Romalis M, Ledbetter M. Phys Rev Lett. 2001; 87:067601. [PubMed: 11497862]
3. Springuel-Huet MA, Bonardet JL, Gédéon A, Fraissard J. Magn Reson Chem. 1999; 37:S1.
4. Schröder L, Lowery TJ, Hilty C, Wemmer DE, Pines A. Science. 2006; 314:446. [PubMed: 17053143]
5. Spence MM, Rubin SM, Dimitrov IE, Ruiz EJ, Wemmer DE, Pines A, Yao SQ, Tian F, Schultz PG. Proc Natl Acad Sci U S A. 2001; 98:10654. [PubMed: 11535830]
6. Lowery TJ, Rubin SM, Ruiz EJ, Spence MM, Winssinger N, Schultz PG, Pines A, Wemmer DE. Magn Reson Imaging. 2003; 21:1235. [PubMed: 14725931]
7. Wolber J, Cherubini A, Leach MO, Bifone A. Magn Reson Med. 2000; 43:491. [PubMed: 10748422]
8. Navon G, Song YQ, Rõõm T, Appelt S, Taylor RE, Pines A. Science. 1996; 271:1848.
9. Driehuys B, Cofer GP, Pollaro J, Boslego J, Hedlund LW, Johnson GA. Proc Natl Acad Sci U S A. 2006; 103:18278. [PubMed: 17101964]
10. Walker TG, Happer W. Rev Mod Phys. 1997; 69:629.
11. Driehuys B, Cates G, Miron E, Sauer K, Walter D, Happer W. Appl Phys Lett. 1996; 69:1668.
12. Zook AL, Adhyaru BB, Bowers CR. J Magn Reson. 2002; 159:175. [PubMed: 12482697]
13. Nikolaou P, Whiting N, Eschmann NA, Chaffee KE, Goodson BM, Barlow MJ. J Magn Reson. 2009; 197:249. [PubMed: 19162517]
14. Bhaskar ND, Happer W, McClelland T. Phys Rev Lett. 1982; 49:25.
15. Nelson IA, Walker TG. Phys Rev A. 2001; 65:012712.
16. Norquay G, Parnell SR, Xu X, Parra-Robles J, Wild JM. J Appl Phys. 2013; 113:044908.
17. Ruset IC, Ketel S, Hersman FW. Phys Rev Lett. 2006; 96:053002. [PubMed: 16486926]
18. Imai H, Fukutomi J, Kimura A, Fujiwara H. Concept Magn Reson B. 2008; 33:192.
19. Korchak SE, Kilian W, Mitschang L. Appl Magn Reson. 2013; 44:65. [PubMed: 23349565]
20. Rosen M, Chupp T, Coulter K, Welsh R, Swanson S. Rev Sci Instrum. 1999; 70:1546.
21. Schrank G, Ma Z, Schoeck A, Saam B. Phys Rev A. 2009; 80:063424.
22. Walter D, Griffith W, Happer W. Phys Rev Lett. 2001; 86:3264. [PubMed: 11327946]
23. Hersman FW, et al. Acad Radiol. 2008; 15:683. [PubMed: 18486005]
24. Nikolaou P, et al. Proc Natl Acad Sci U S A. 2013; 110:14150. [PubMed: 23946420]
25. Mann D, Broida H. J Appl Phys. 1973; 44:4950.
26. Atutov S, Plekhanov A, Shalagin A, Calabrese R, Tomassetti L, Guidi V. Eur Phys J D. 2012; 66:140.
27. Wagshul ME, Chupp TE. Phys Rev A. 1989; 40:4447. [PubMed: 9902687]
28. Drake, G. Atomic, Molecular and Optical Physics Handbook. AIP; New York: 1996.
29. Romalis MV, Miron E, Cates GD. Phys Rev A. 1997; 56:4569.
30. Fink A, Brunner E. Appl Phys B. 2007; 89:65.

31. Nelson, I.; Driehuys, B.; Kadlecek, S. 12th Annual Scientific Meeting; 2004; p. 1689
32. Krause L. Appl Optics. 1966; 5:1375.
33. Babcock E, Nelson I, Kadlecek S, Driehuys B, Anderson LW, Hersman FW, Walker TG. Phys Rev Lett. 2003; 91:123003. [PubMed: 14525358]
34. Wagshul M, Chupp T. Phys Rev A. 1994; 49:3854. [PubMed: 9910682]
35. Rosenberry MA, Reyes JP, Tupa D, Gay TJ. Phys Rev A. 2007; 75:023401.
36. Saha I, Nikolaou P, Whiting N, Goodson BM. Chem Phys Lett. 2006; 428:268.
37. Lancor B, Babcock E, Wyllie R, Walker T. Phys Rev A. 2010; 82:043435.
38. Chann B, Babcock E, Anderson L, Walker T. Phys Rev A. 2002; 66:033406.
39. De Heer W, Milani P, Châtelain A. Zeitschrift für Physik D Atoms, Molecules and Clusters. 1991; 19:241.
40. Sun Q, Wang Q, Wang S. Phys Lett A. 1997; 228:297.
41. Papanikolaou N, Stefanou N, Zeller R, Dederichs P. Phys Rev Lett. 1993; 71:629. [PubMed: 10055324]
42. de Heer WA, Selby K, Kresin V, Masui J, Vollmer M, Chatelain A, Knight W. Phys Rev Lett. 1987; 59:1805. [PubMed: 10035336]
43. Bhaskar N, Frueholz R, Klimcak C, Cook R. Phys Rev B. 1987; 36:4418.
44. Martin T. J Chem Phys. 1984; 81:4426.
45. Alexandrov E, Balabas M, Budker D, English D, Kimball D, Li CH, Yashchuk V. Phys Rev A. 2002; 66:042903.
46. Gozzini A, Mango F, Xu J, Alzetta G, Maccarrone F, Bernheim R. Nuovo Ciment D. 1993; 15:709.
47. Burchianti A, et al. Europhys Lett. 2004; 67:983.
48. Li Y, Blaisten-Barojas E, Papaconstantopoulos D. Phys Rev B. 1998; 57:15519.
49. Witte C, Kunth M, Rossella F, Schröder L. J Chem Phys. 2014; 140:084203. [PubMed: 24588160]
50. Whiting N, Nikolaou P, Eschmann NA, Goodson BM, Barlow MJ. J Magn Reson. 2011; 208:298. [PubMed: 21185208]
51. Mochizuki S, Inozume K, Ruppin R. J Phys-Condens Mat. 1999; 11:6605.
52. Baranga ABA, Appelt S, Romalis MV, Erickson CJ, Young AR, Cates GD, Happer W. Phys Rev Lett. 1998; 80:2801.
53. Babcock E, Chann B, Walker T, Chen W, Gentile T. Phys Rev Lett. 2006; 96:083003. [PubMed: 16606177]
54. Singh J, et al. arXiv preprint arXiv:1309.4004. 2013
55. Chen WC, Gentile TR, Ye Q, Walker TG, Babcock E. J Appl Phys. 2014; 116:014903.
56. Chen W, Gentile T, Walker T, Babcock E. Phys Rev A. 2007; 75:013416.
57. Ruset, IC. PhD dissertation. University of New Hampshire; 2005.

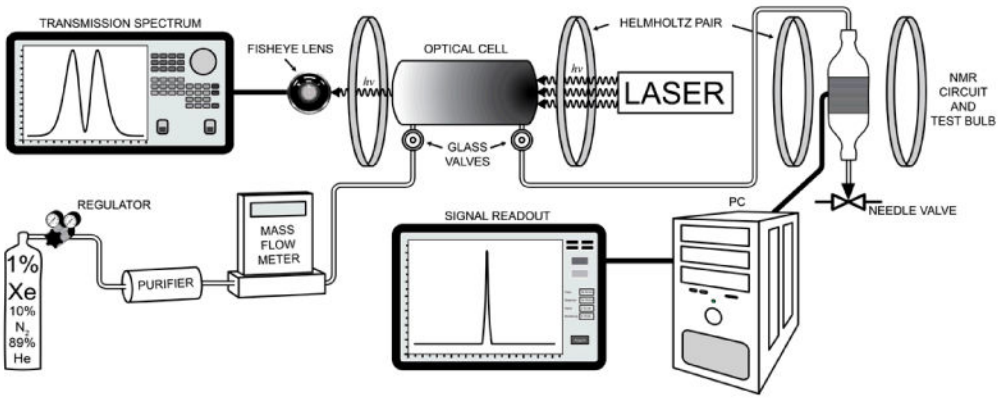

Figure 1.

Apparatus to generate polarization vs. flow curves. It consists of a standard SEOP polarizer that flows directly to an adjacent NMR test bulb housed in a 20 gauss magnetic field where ^{129}Xe polarization is sampled by a low-frequency NMR circuit and digitized using the computer and NMR software. Laser absorption is monitored and quantified using an on-board spectrometer and photodiode. Xenon flow rate through the system is controlled by a needle valve downstream from the test bulb.

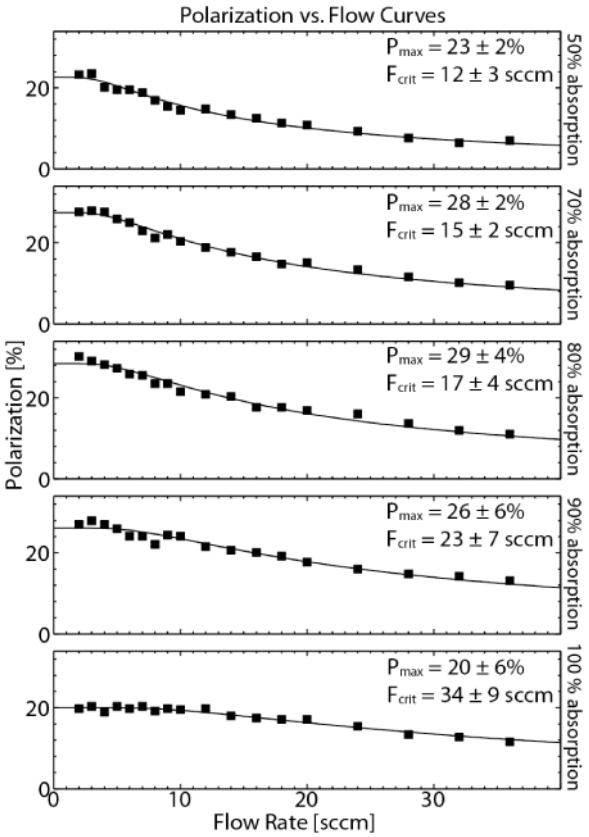

Figure 2.

Representative ^{129}Xe polarization vs. flow curves acquired in the 300-cc cell using the line-narrowed laser at 5 different levels of absorption. Each of these curves can be fit to estimate peak ^{129}Xe polarization P_0 and production rate F_{crit}.

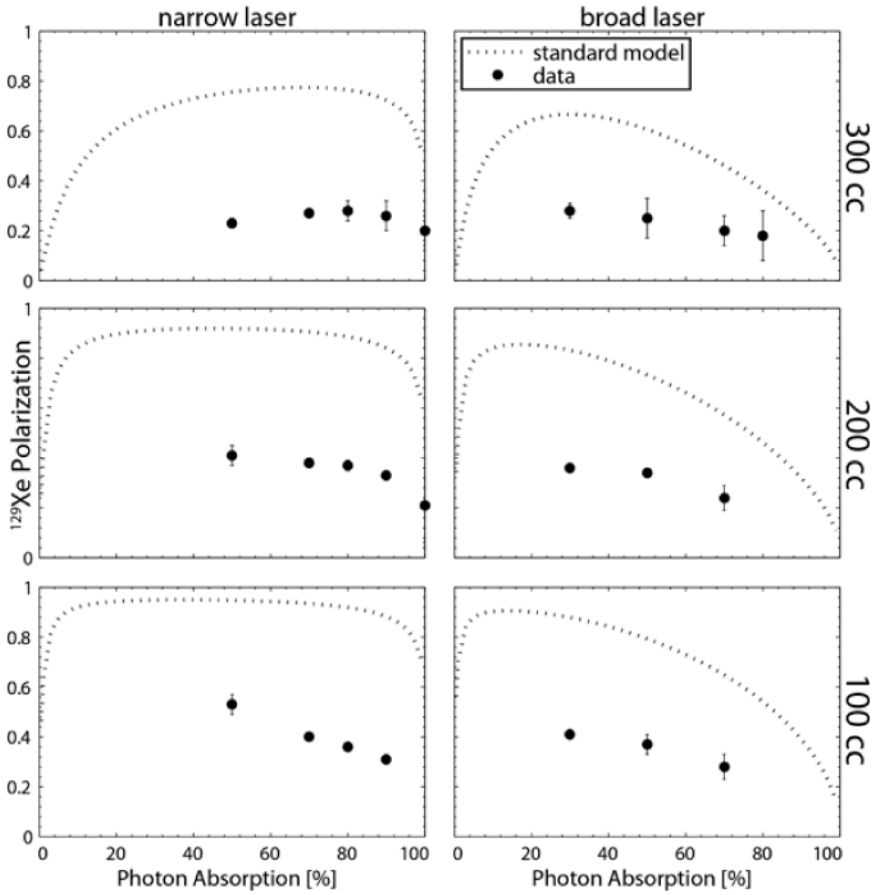

Figure 3.

Peak ^{129}Xe polarization achieved for all 3 cell types and pumped with both types of lasers at numerous absorption levels. Each point is the result of a single flow curve. Overlaid in the plot is the polarization predicted by the standard SEOP model.

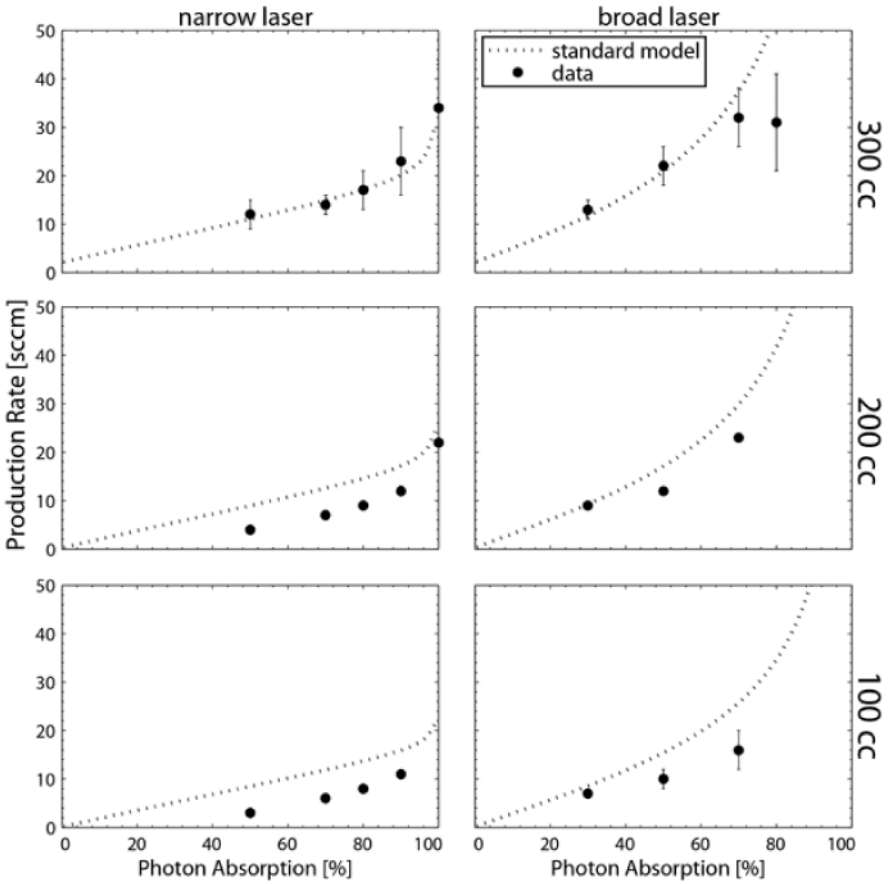

Figure 4.

Critical flow rates extracted from fitting the same flow curves as used to obtain peak polarization depicted in Fig. 3. These values are compared to predictions of the standard SEOP model and show significant underproduction, particularly for the smaller cells and high absorption.

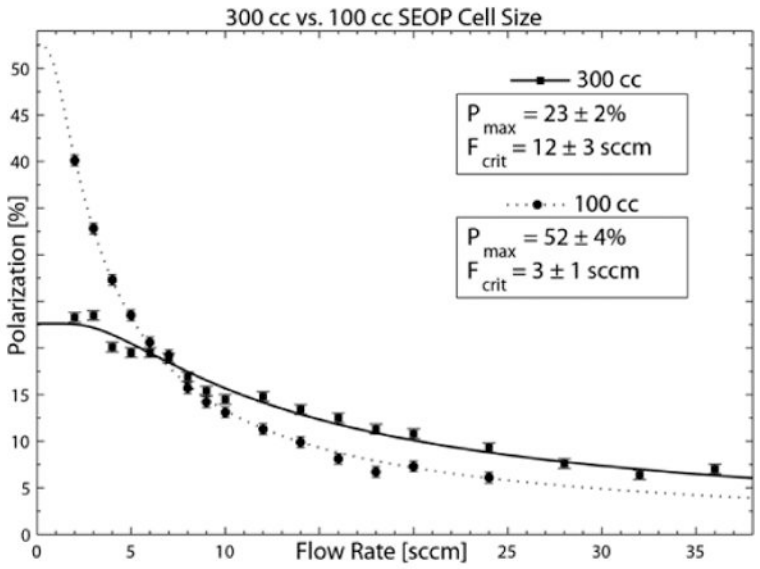

Figure 5.

Comparison of polarization vs. flow curves obtained when pumping the 100-cc and 300-cc cells with the narrowed laser, each absorbing 50% of the available light. This illustrates that although higher polarization can be achieved in the smaller cell, it comes with an unexpected 4-fold penalty in production rate.

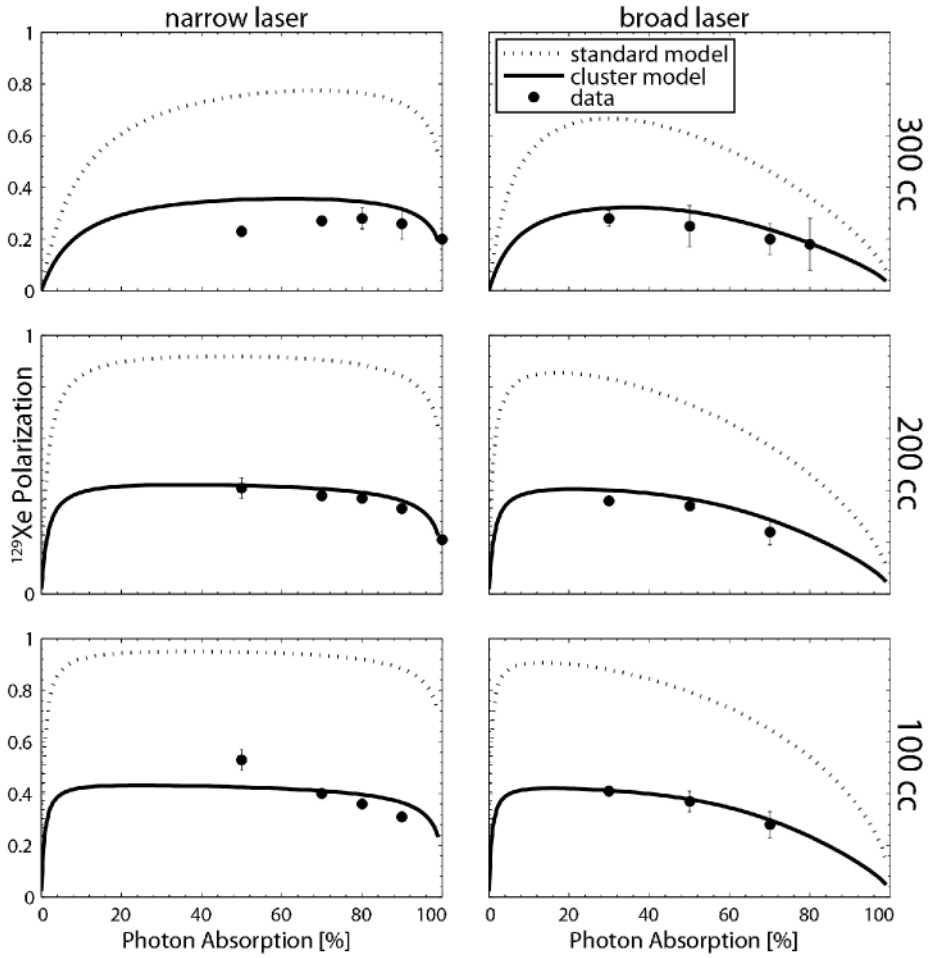

Figure 6.

^{129}Xe peak polarization data from Figure 3, but now including predictions of the cluster model (bold) showing significantly better agreement than the standard SEOP model (dotted).

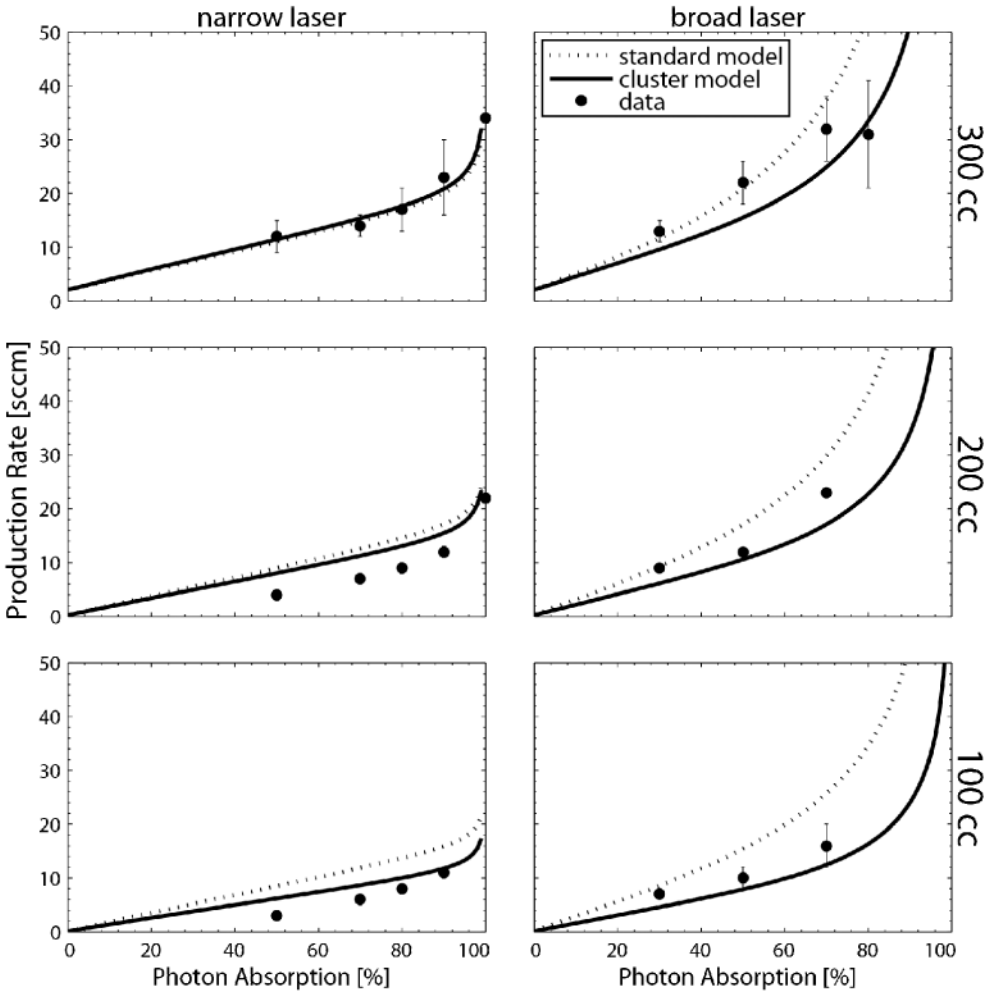

Figure 7.

^{129}Xe production rates from Figure 4, now compared to the cluster model (bold), which shows considerably better agreement across absorption levels than the standard model (dotted).

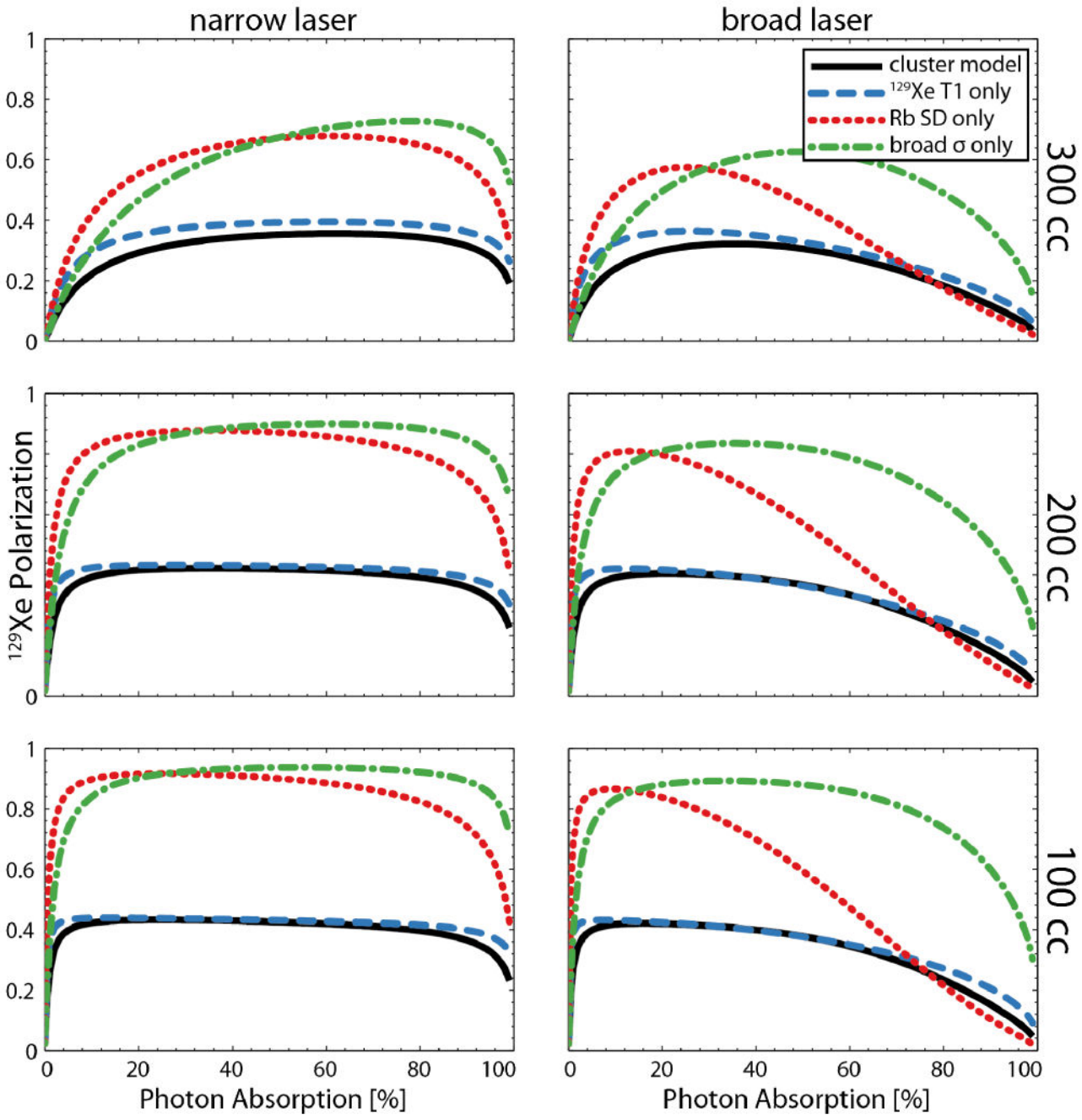

Figure 8.

(Color online) ^{129}Xe peak polarization data from the cluster model in Figure 6 (black), but now including predictions of the individual effects of the model, that is, the standard model with only the addition of the ^{129}Xe T1 relaxation effect (blue), Rb spin destruction effect (red) and broad photon absorption effect (green).

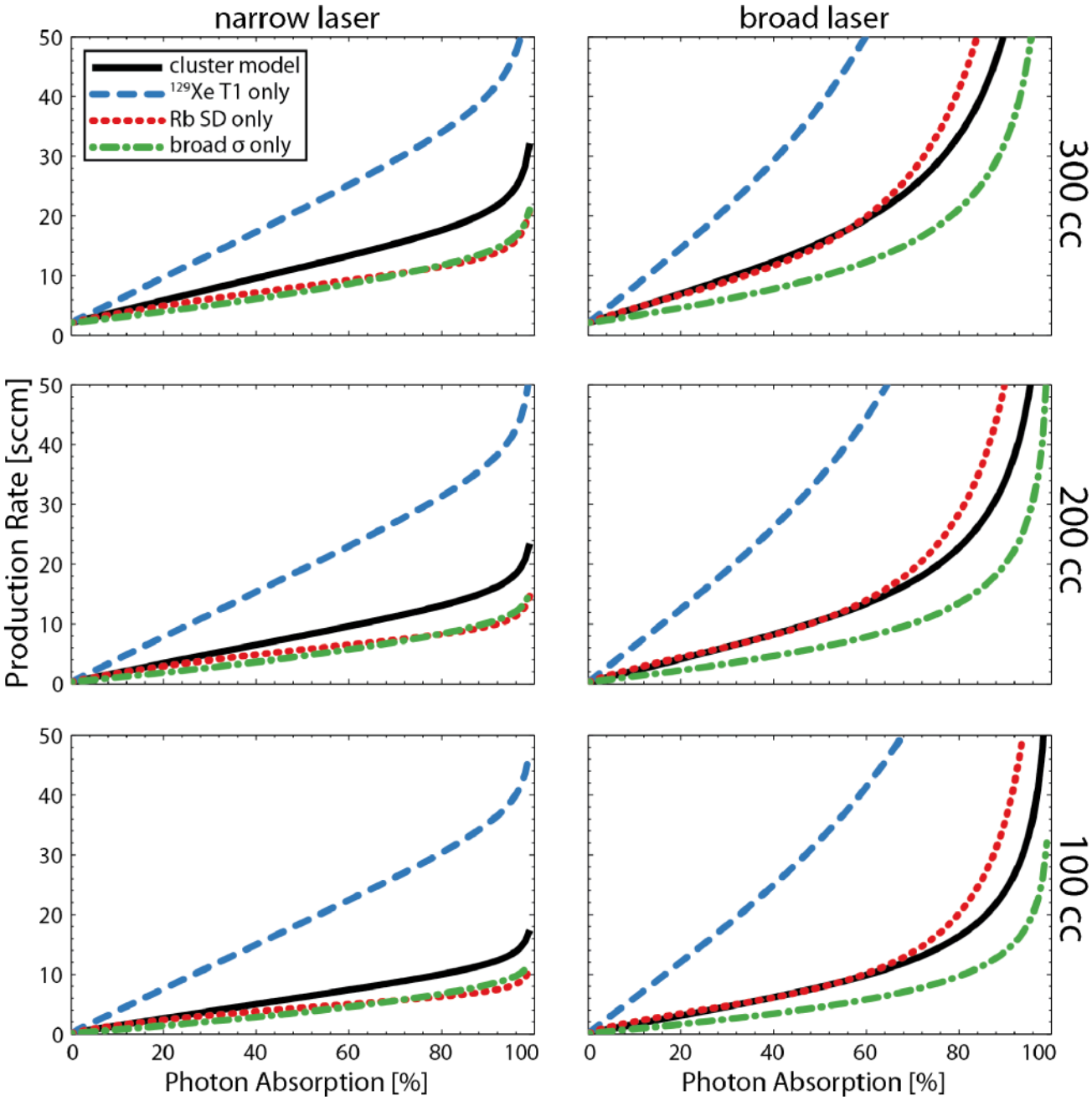

Figure 9.

(Color online) ^{129}Xe production rates from Figure 7, but now including predictions of the individual effects of the model, ^{129}Xe T1 relaxation (blue), Rb spin destruction (red) and broad photon absorption (green) as compared to the full cluster model (black).

Table I

Characteristics of the optical cells used in this work. Cell T_1 measured in pure Xe at STP.

V [cm^3]	l [cm]	r [cm]	A [cm^2]	T_1 [min]
100	9.0	1.9	130	56
200	12.5	2.25	210	43
300	12.7	2.71	260	8

Table II

Proposed cluster scaling constant, cluster relaxation cross-sections, and scattering cross-section determined from steepest descent fit.

$\Theta_{cluster}$	$\langle \sigma_{cluster-Rb}\, v \rangle$	$\langle \sigma_{cluster-Xe}\, v \rangle$	$\sigma_{cluster}$
6.5×10^{-8} s	4×10^{-7} cm^{3}s^{-1}	4×10^{-13} cm^{3}s^{-1}	1×10^{-12} cm^2